

# MPSN: Motion-aware Pseudo Siamese Network for Indoor Video Head Detection in Buildings

Kailai Sun<sup>a,1</sup>, Xiaoteng Ma<sup>a,1</sup>, Peng Liu<sup>a,1</sup> and Qianchuan Zhao<sup>a,\*</sup>

<sup>a</sup>Center for Intelligent and Networked Systems, Department of Automation, BNRist, Tsinghua University, Beijing, 100084, China

## ARTICLE INFO

### Keywords:

Indoor video head detection  
Building occupancy detection  
Motion estimation  
Deep features aggregation  
Adversarial attack

## ABSTRACT

Head detection in the indoor video is an essential component of building occupancy detection. While deep models have achieved remarkable progress in general object detection, they are not satisfying enough in complex indoor scenes. The indoor surveillance video often includes cluttered background objects, among which heads have small scales and diverse poses. In this paper, we propose **Motion-aware Pseudo Siamese Network (MPSN)**, an end-to-end approach that leverages head motion information to guide the deep model to extract effective head features in indoor scenarios. By taking the pixel-wise difference of adjacent frames as the auxiliary input, MPSN effectively enhances human head motion information and removes the irrelevant objects in the background. Compared with prior methods, it achieves superior performance on the two indoor video datasets. Our experiments show that MPSN successfully suppresses static background objects and highlights the moving instances, especially human heads in indoor videos. We also compare different methods to capture head motion, which demonstrates the simplicity and flexibility of MPSN. Finally, to validate the robustness of MPSN, we conduct adversarial experiments with a mathematical solution of small perturbations for robust model selection. Code is available at <https://github.com/pl-share/MPSN>.

## 1. INTRODUCTION

The human dimension information plays a significant role in efficient building energy-saving and comfortable indoor environments (Salimi and Hammad, 2019; Sun, Zhao and Zou, 2020). Recent studies showed that control strategies based on occupancy information can save building energy by approximately 20–45% (Pang, Chen, Zhang, O'Neill, Cheng and Dong, 2020), and improve thermal comfort by 29.1%. In particular, occupancy information ensures a closed-loop feedback strategy (Zou, Zhao, Yang and Wang, 2017) to control building Heating, Ventilation, and Air-Conditioning (HVAC) and lighting systems.

Vision-based occupancy detection has recently become a hot research topic to obtain accurate and robust occupancy information in buildings (Sun et al., 2020; Choi, Um, Kang, Kim and Kim, 2021b). These methods are mainly divided into three categories: body, face, and head detection. Head detection has been the perceived center point of people detection in complex indoor scenes. The limitations of body and face detection methods have gradually been exposed. Specifically, body detection methods extract the body features for recognition, which suffers from inter-class and intra-class occlusions (Chi, Zhang, Xing, Lei, Li and Zou, 2020). Face detection methods rely on facial features, but fail when the person to be detected is turned backward (Khan, Altamimi, Ullah, Ullah and Cheikh, 2020). Compared with

the former two methods, head detection has a wider range of applications because human heads are visible and reliable in complex indoor scenes. In particular, indoor occupancy detection methods in buildings (Trivedi and Badarla, 2020; Zou et al., 2017; Sun, Zhao, Zhang and Hu, 2022) focus on the head part instead of the whole human body on account of the severe occlusion.

Although many exist head detectors make great progress in general scenes (Vu, Osokin and Laptev, 2015; Granger, Kiran, Blais-Morin et al., 2017; Liu, Zhang, Xie, Wei, Wang and Niu, 2021a), the detection task is still challenging in the indoor scene. As shown in Fig. 1, many background objects (e.g., black bags, balls, flowers) have head-like sizes, colors, and textures, resulting in a high false-positive rate (FPR). On the other hand, due to the relatively small scales, it is hard to detect heads with a high confidence score in crowded scenes. Moreover, the moving head causes significant variations in scale, pose, texture, and illumination, which increases the false-negative rate (FNR). Researches on multi-scale features (Liu, Zhang, Bian, Zhang and Cheng, 2021b) and attention mechanisms (Woo, Park, Lee and Kweon, 2018; Shen, Qin and Zeng, 2019) are developed to handle the multi-scale objects and similar background objects. However, existing studies mainly focus on head detection in static images (Meng, Li, Liu, Xu and Ji, 2020; Khan, Ullah, Uzair, Ullah, Ullah and Cheikh, 2019; Stewart, Andriluka and Ng, 2016), which are not satisfying enough in the indoor video scenarios.

To solve these issues, we notice that human heads are often on the move while the background objects are almost always static. We ask: *can we utilize the motion of human heads to enhance the features while suppressing background information?* This work gives us a confirmatory answer. The head motion information is captured by the difference of adjacent frames. It is sensitive to moving objects even though they are small in complex scenes. Besides, the motion

\*Corresponding author.

✉ sk118@mails.tsinghua.edu.cn (K. Sun);

ma-xt17@mails.tsinghua.edu.cn (X. Ma);

liup20@mails.tsinghua.edu.cn (P. Liu);

zhaoqc@mail.tsinghua.edu.cn (Q. Zhao)

ORCID(s): 0000-0003-1648-3409 (K. Sun);

0000-0002-7250-6268 (X. Ma); 0000-0002-7952-5621 (Q.

Zhao)

<sup>1</sup>These authors contributed equally to this work.

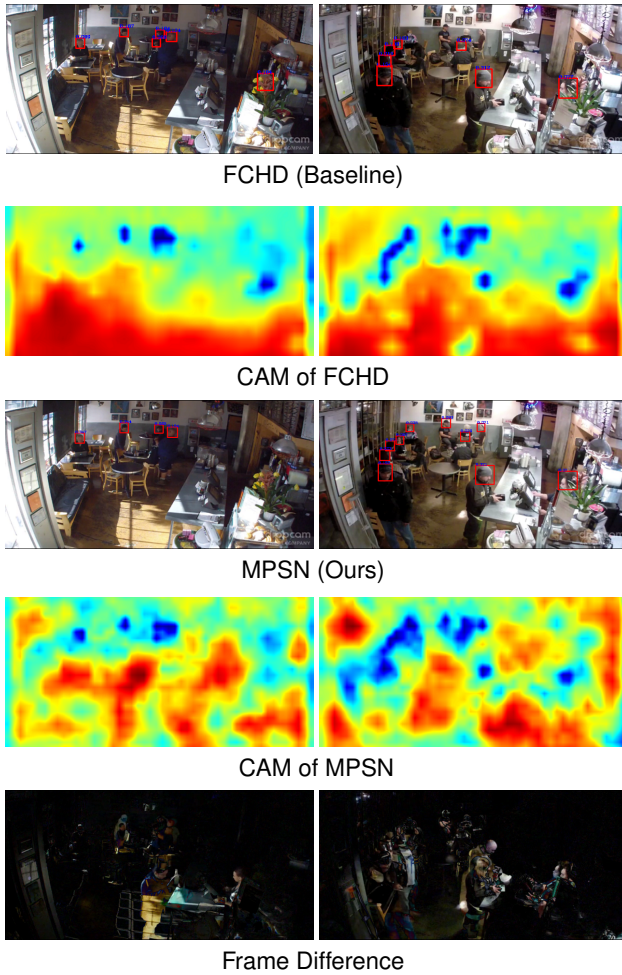


**Figure 1:** Comparison of MPSN with the baseline method FCHD (Meng et al., 2020). Two columns show two respective instances in the crowd Brainwash dataset (Stewart et al., 2016). In the first column, when there exist similar objects (flowers), MPSN can suppress the static regions and filter many false positives. In the second column, the single image detector fails to propose accurate boxes when heads are small. Our MPSN can enhance the motion regions and reduce many false negatives. For interpretation purposes, we visualize the feature (heatmaps) of the last CNN layer which are generated by the Class Activation Map (CAM) method (Zhou et al., 2016). Deep blue regions of the heatmaps represent the locations of heads in the feature space.

information has the ability to filter static objects. If we suppress static instances while enhancing moving instances, the FPR and FNR will be effectively reduced.

In this work, we propose **Motion-aware Pseudo Siamese Network (MPSN)** for indoor video head detection, an accurate and flexible framework for video head detection. It can robustly detect head regions in a sequence of frames, even when the time intervals of frames are large. First, we extract the frame difference features between neighboring frames, which is sensitive to motion regions (see Fig. 1 for examples in the real dataset). Second, we propose a pseudo siamese network to extract the similar features between frame difference and original image. Third, these features are aggregated with a constraint, which can suppress false

positives and recover false negatives. Finally, detection methods, such as region proposal network (RPN) (Ren, He, Girshick and Sun, 2015), are cascaded to generate proposal head boxes.

To our best knowledge, MPSN is the first work to jointly train the current frame and motion information into an end-to-end CNN network in head detection. This work aims to solve the problems in the indoor video head detection, such as similar static objects and diverse head samples. The contributions of this paper include: 1) We propose a pixel-level motion-aware pseudo siamese network to learn the more robust head features. 2) With more effective motion features, we demonstrate the MPSN on the crowd Brainwash dataset (Stewart et al., 2016) and the Restaurant dataset (El Ahmar, Erlik Nowruzi and Laganieri, 2020) with superior performance and low memory requirement. 3) As a general head detection framework, we demonstrate the flexibility of MPSN with different backbone networks (VGGNet16 (Simonyan and Zisserman, 2015), MobileNetv2 (Sandler, Howard, Zhu, Zhmoginov and Chen, 2018), Resnet18 (He, Zhang, Ren and Sun, 2015)). 4) To evaluate the robustness of MPSN, we implement adversarial samples to MPSN, and provide the mathematical solution of small perturbations to select more robust models.

## 2. RELATED WORK

### 2.1. Generic Object Detection

In recent years, deep learning technologies (e.g., CNN and transformer) have achieved state-of-the-art performances in object detection tasks. Generally speaking, these methods based on CNN can be divided into two categories: the two-stage approach and the one-stage approach. The two-stage methods, such as RCNN (Tien, Wei, Calautit, Darkwa and Wood, 2022) and R-FCN (Dai, Li, He and Sun, 2016), usually propose enough ROI (region of interest) boxes that contain potential objects, predict them as specific categories, refine the offsets and scales of bounding boxes. The one-stage methods, such as YOLO (Wang, Huang, Feng, Cao and Haghghat, 2021), SSD (Ke, Zhuang, Pu and Wang, 2020), and CenterNet (Duan, Bai, Xie, Qi, Huang and Tian, 2019), usually jointly predict the probability scores and regress bounding boxes together. The two-stage methods can achieve higher accuracy, while the one-stage methods have less computational complexity. Recently, DETR (Dai, Chen, Yang, Zhang, Yuan and Zhang, 2021) directly utilizes transformer decoder and bipartite matching strategies to predict the joint class, position, and bounding boxes. However, transformer networks require a large number of training parameters and samples, which hinders the deployment on resource-constrained environment (Khan, Naseer, Hayat, Zamir, Khan and Shah, 2021).

### 2.2. Video Object Detection

Many novel challenges appear when directly applying the general detectors to videos. The detection performance suffers from motion blur, video defocus, and rare poses. Studies on video object detection can be divided into two

categories: box-level approach and pixel-level approach. Box-level approaches aim to refine the final results by designing hand-crafted box-level rules between neighboring frames (Jia, Zhang and Liu, 2019; Han, Khorrami, Paine, Ramachandran, Babaeizadeh, Shi, Li, Yan and Huang, 2016). But these box-level methods only rely on single detectors and are not optimized jointly. Few pixel-level methods (Wang, Zhou, Yan and Deng, 2018; Zhu, Dai, Yuan and Wei, 2018) are proposed to aggregate deep temporal features with optical flow. However, in complex scenes, methods based on optical flow face significant challenges when the object changes rapidly or moves quickly (Wang et al., 2018).

### 2.3. Indoor Head Detection

Most related studies treat indoor head detection as a subtask of object detection. Early methods utilized hand-crafted features (Haar Features (Viola and Jones, 2001), Aggregate Channel Features (Chandran, Wong and Ieee, 2016), HOG Features (Zou et al., 2017), etc.) and classifiers to detect human heads. With the rapid development of deep learning, the mainstream of head detection method switches to the CNN-based object detection method (Stewart et al., 2016; Chouai, Dolezel, Stursa and Nemecek, 2021; Khan, Ali, Zafar and Noorwali, 2020; Khan et al., 2020; Babu Sam, Surya and Venkatesh Babu, 2017).

In practice, different from generic objects, human heads have special properties. Thus, the specific anchor size selection strategy (Meng et al., 2020), multi-scale features aggregation strategy (Vu et al., 2015; Xiang and Zhu, 2017), attention selection strategy (Li, Wang, Wang, Tai, Qian, Yang, Wang, Li and Huang, 2019; Shen et al., 2019), and the relationship between heads and people matching strategy (Chi et al., 2020) can effectively improve the detection performance.

### 2.4. Indoor Occupancy Detection

Indoor occupancy detection is a challenging task involving object detection, head detection, video analysis, etc. Studies (Huang and Hao, 2020; Mutis, Ambekar and Joshi, 2020; Choi, Um, Kang, Kim and Kim, 2021a) used general object detectors (YOLO, Faster RCNN, etc.) to detect indoor occupancy. However, the indoor scenes are extremely complex, resulting in human bodies occluded by desks, chairs, and other people. Therefore, to avoid the severe occlusion problem, occupancy detection methods based on head detection have been developed (Meng et al., 2020; Zou et al., 2017; Guan and Huang, 2015; Acquaah, Steele, Gokaraju, Tesiero and Monty, 2020). In addition, object/head detection methods can be cascaded with video analysis technologies to obtain higher detection performance (Sun et al., 2022; Benezeth, Laurent, Emile and Rosenberger, 2011; Aftab, Chen, Chau and Rahwan, 2017; Dino, Kalfaoglu, Sari, Akin, Iseri, Alatan, Kalkan and Erdogan, 2019).

## 3. Method

Given an image head detection task, we have a feature extraction network  $N_{feat}$ , and a detection network  $N_{det}$ . The

output for input image  $I$  is  $y = N_{det}(h)$ , where  $h = N_{feat}(I)$ . The key idea of this paper is to apply motion information to suppress static background objects and focus on the head instances in the pixel level.

The inference pipeline is depicted in Fig. 2, consisting of four modules: 1) The *motion estimation* module is developed to estimate the head motion information, which is fed to the pseudo siamese network. 2) The *feature aggregation* module is proposed to extract robust head motion features. 3) The *gradient backpropagation* module can explain the gradient principle of MPSN. 4) Finally, the *detection network* module decodes the aggregated features to head boxes.

### 3.1. Motion estimation

As mentioned in Section 1, the human head would not be static for a long time. We introduce prior motion knowledge to guide the network  $N_{feat}$  to extract effective head features. For further applications, we use simple BS methods to extract motion areas roughly. We define the frame difference operator as

$$I_{df} = |I_f - I_{f-1}|, f = 1, \dots, N, \quad (1)$$

where  $I_f$  is the  $f$ th frame in an image sequence, and  $N$  is the sequence length. Although the time intervals between  $I_{f+1}$  and  $I_f$  have large variations in applications, this operator is sensitive to motion pixels and contains spatial location information.

In addition, optical flow has been widely applied in video analysis. It helps to estimate video motion information. In this paper, we define the motion field by the optical flow estimation algorithm  $\mathcal{F}$  (Teed and Deng, 2020; Ilg, Mayer, Saikia, Keuper, Dosovitskiy and Brox, 2017; Lucas, Kanade et al., 1981) as

$$I_{df} = \mathcal{F}(I_f, I_{f-1}), f = 1, \dots, N, \quad (2)$$

The rough motion features will be further extracted by the following pseudo siamese network.

### 3.2. Feature aggregation

The original frame  $I_f$  and frame difference image  $I_{df}$  are parallelly fed to the feature extraction network  $N_{feat}$ . In other words, the inputs of the  $N_{feat}$  are two images, and the output is the aggregated features  $h_{agg}$ .

Many siamese CNN architectures can support the double inputs for similarity comparison (Wu, Zhang, Zhang, Zhang, Wang, Zhang and Sun, 2020) or regression (Held, Thrun and Savarese, 2016), whose weights are shared between the parallel streams. However, the motion is specifically extracted defined in Eq. (1), which has an excellent appearance difference from the original frame. Considering they lie on different manifolds, the siamese CNN is not suitable for our task. We design a novel pseudo siamese network (Hughes, Schmitt, Mou, Wang and Zhu, 2018) to handle this issue.

First, the pseudo siamese network is used to extract similar features between  $I_f$  and  $I_{df}$ . The pseudo siamese

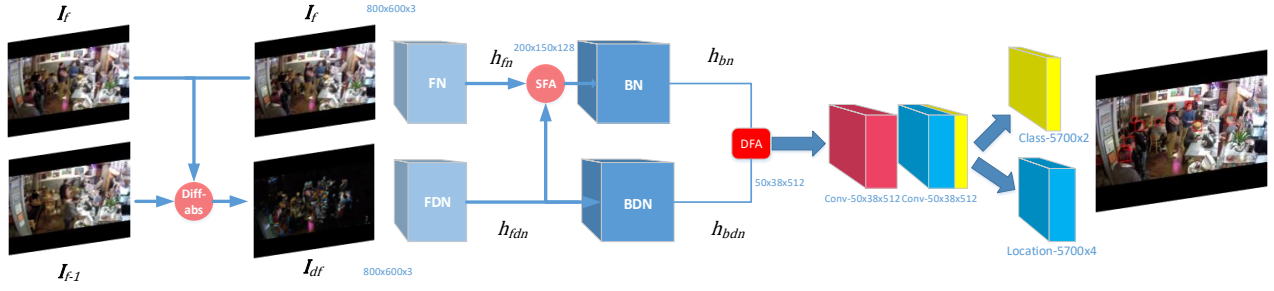


**Figure 2:** The framework of MPSN. Firstly, the original frame  $I_f$  and the frame difference  $I_{df}$  are parallelly fed to the pseudo siamese network. The paired networks (FN and FDN, BN and BDN) have the same architectures but different weights. Secondly, the features are aggregated with our SFA and DFA at different pixel levels. Finally, the boxes and classes are predicted simultaneously with RPN.

network can ensure the size and channel are completely equal at the same level layers. The architectures of the two sub-networks are totally the same, while the weights are learned separately. In Fig. 2, the front network (FN) corresponds to the front difference network (FDN) while the back network (BN) corresponds to the back difference network (BDN). Then,  $N_{feat} = \{N_{FN}, N_{FDN}, N_{BN}, N_{BDN}\}$ . The shape of features  $h_{fn}$  is equal to the features  $h_{fdn}$ 's:

$$\begin{aligned} h_{fn} &= N_{FN}(I_f) \\ h_{fdn} &= N_{FDN}(I_{df}). \end{aligned} \quad (3)$$

Second, to improve the accuracy and robustness of human head detection, the network should focus on moving areas that contain human heads. In order to enhance the motion regions and suppress the non-moving regions, we present shallow features aggregation (SFA) and deep features aggregation (DFA). The goal of the SFA is to aggregate the shallow features at the low-level layers. To reserve more temporal information, MPSN directly learns the sum of two features after activation functions:

$$SFA : h_{fn} = h_{fdn} + h_{fn}. \quad (4)$$

Intuitively, the motion regions are added to the original features through this simple low-level aggregation. SFA can enhance the small and moving pixels but may be inaccurate when similar background objects exist. In fact, SFA is hard to ensure the activation scores of similar background objects are smaller than human heads'. To further enhance the moving instances and suppress the static background instances, we conduct the DFA on the position-sensitive score maps:

$$\begin{aligned} h_{bn} &= N_{BN}(h_{fn}) \\ h_{bdn} &= N_{BDN}(h_{fdn}) \\ DFA : h_{agg} &= \alpha \cdot h_{bn} \odot \sigma(h_{bdn}) + \beta \cdot h_{bdn}. \end{aligned} \quad (5)$$

In the deep layers, the instance-level features can represent head activation scores. The feature value of  $h_{bdn}$  indicates the spatial intensity of moving heads. At every channel, we resize  $h_{bdn}$  with the sigmoid functions to (0, 1). The scores are multiplied with the features  $h_{bn}$  by element-wise (Hadamard) product in Eq. (5). In other words, the

$\sigma(h_{bdn})$  can be seen as a special mask to activate the local regions of the original features maps  $h_{bn}$ . Unlike normal masks in image processing, this mask is dense and learnable: every value belongs to (0, 1) and is learned from the above pseudo siamese network. This simple operator is powerful because the moving instances will be partly reserved while the static instances will be suppressed.

Note that  $\beta \cdot h_{bdn}$  is added at the Eq. (5). Because the features  $h_{bdn}$  are resized to (0, 1) and the features  $h_{bn}$  are normalized (e.g., Batchnorm, Instancenorm, Layernorm) before activation functions, the activated head features will be decreased. In order to compensate for this loss and enhance the regions of moving heads, we add  $h_{bdn}$  after the element-wise product in Eq. (5).

### 3.3. Gradient backpropagation

The derivatives of DFA are related to the Hadamard product. Construct the diagonal matrix so that the following equation holds.

$$h_{bn} \odot \sigma(h_{bdn}) = \text{Diag}(h_{bn})\sigma(h_{bdn}).$$

Besides, the element-wise function differential is

$$d(\sigma(h_{bdn})) = \sigma(h_{bdn})' \odot d(h_{bdn}).$$

According to the Eq. (5), we can obtain

$$\begin{aligned} \frac{\partial L(\theta, I_f, y_f)}{\partial h_{bdn}} &= \frac{\partial L(\theta, I_f, y_f)}{\partial h_{agg}} \cdot \frac{\partial h_{agg}}{\partial \sigma(h_{bdn})} \cdot \frac{\partial \sigma(h_{bdn})}{\partial h_{bdn}} \\ &= \frac{\partial L(\theta, I_f, y_f)}{\partial h_{agg}} \cdot [\alpha \cdot \text{Diag}(h_{bn}) + \beta \cdot I] \\ &\quad \cdot \text{Diag}[\sigma(h_{bdn}) \odot (1 - \sigma(h_{bdn}))], \end{aligned} \quad (6)$$

where the  $I$  is the identity matrix, and the  $\mathbf{1}$  is the all-ones matrix.

### 3.4. Detection network

Many detectors can be used after the backbone network for head detection, such as RPN and DETR.

$$y_f = N_{det}(h_{agg}), \quad (7)$$

**Table 1**

The comparison of MPSN against other methods on the Brainwash dataset and the Restaurant dataset.

Dataset	Method	Backbone	$AP_{50}$
Brainwash	ReInspect	GoogLeNet	0.78
	SSD	ResNet101	0.80
	DETR	ResNet18	0.53
	FCHD	VGGNet16	0.70
	MPSN	MobileNetv2	<b>0.90</b>
	MPSN	VGGNet16	<b>0.91</b>
Restaurant	YOLOX	CSPNet	0.83
	HTC++	Swin-B	0.68
	SSD	ResNet18	0.51
	FCHD	VGGNet16	0.75
	MPSN	MobileNetv2	<b>0.84</b>
	MPSN	VGGNet16	<b>0.86</b>

where the output  $y$  represents the head boxes and classes. Our detection network is based on FCHD (Meng et al., 2020) and DETR (Carion, Massa, Synnaeve, Usunier, Kirillov and Zagoruyko, 2020). For FCHD, we have made some modifications: 1) the backbone network is replaced with our proposed pseudo siamese network with normalization; 2) we add an Additive Penultimate CNN (APC) layer before regressing coordinates and classification in Fig. 2; 3) we select three anchors of size 16x16, 32x32, and 64x64; 4) in order to balance the foreground-background class, we use the focal loss (Lin, Goyal, Girshick, He and Dollár, 2017) instead of the standard cross-entropy loss. As for DETR, we only modify the backbone network and keep the transformer unchanged for comparison.

## 4. Experiments and discussions

First, we compare MPSN with various methods on two public indoor crowd datasets in Section 4.1. Considering SFA, DFA, and APC can be embedded in most CNN-based models, we mainly focus on the flexibility and comparison study (in Section 4.2, 4.3, and 4.4). Based on different backbone networks and detectors, we show that MPSN can recover missed heads and filter the false background positives, giving a significant performance boost. After comparison, we choose the best model to count indoor occupants, balancing the low computational complexity and high accuracy (in Section 4.5). In addition, adversarial samples are implemented to evaluate the robustness of MPSN (in Section 4.6). Finally, we also provide the mathematical solution of small perturbations to select more robust models.

### 4.1. Datasets

In order to evaluate MPSN, we test the publicly available Brainwash crowd dataset (Stewart et al., 2016) and Restaurant dataset (El Ahmar et al., 2020). For the evaluation metrics, we use the standard average precision ( $AP_{50}$ ). The Brainwash dataset includes 11917 images with 91146 labeled people, in which the test set contains 484 images. The Restaurant dataset was collected in four different indoor

**Table 2**

Comparison of MPSN against the single frame and two frames method among different backbones on two datasets.

Dataset	Method	VGGNet16	MobileNetv2	ResNet18
Brainwash	Single frame	0.876	0.828	0.855
	Two frames	0.868	0.821	0.857
	MPSN	<b>0.878</b>	<b>0.890</b>	<b>0.885</b>
Restaurant	Single frame	0.750	0.785	0.769
	Two frames	0.782	0.808	0.768
	MPSN	<b>0.857</b>	<b>0.838</b>	<b>0.802</b>
Parameters		123.8M	6.7M	24.9M

locations at a restaurant. It includes 1610 images, from which the test set contains 123 images. The images are extracted from the video with a large time interval, thus having significant diversity and difference. Fortunately, the camera is stable, and therefore the proposed motion estimation method is applicable.

### 4.2. Comparison with baselines

To compare the state-of-the-art methods, we test the AP among different methods on two datasets in Table 1. The detailed network architectures and hyperparameters are put in Appendix.

The authors who published the Brainwash dataset (Stewart et al., 2016) provided a baseline detection method named ReInspect. SSD (Ke et al., 2020) algorithm uses multi-scale feature maps to achieve high detection accuracy. FCHD is a fast and accurate head detector with a specific anchor size selection strategy. HTC++ framework (Chen, Pang, Wang, Xiong, Li, Sun, Feng, Liu, Shi, Ouyang et al., 2019) combines detection and segmentation tasks into a joint multi-stage processing and utilizes spatial context to further boost the performance. YOLOX (Ge, Liu, Wang, Li and Sun, 2021) is a high-performance anchor-free detector through integrating YOLO series. To simplify detection pipelines and bypass surrogate tasks, DETR directly utilizes the transformer for object sequence prediction.

Compared with the prior methods, our proposed method, MPSN, achieves the best performance accuracy in the both datasets. Considering the MobileNetv2 backbone (Sandler et al., 2018) has fewer parameters and lower computational complexity, we use it as the default backbone in further discussion.

### 4.3. Flexibility of MPSN

To sufficiently evaluate the flexibility, we conduct three experiments based on FCHD. Table 2 summarizes the performance on two datasets. We select the best model on the evaluation dataset ( $valAP_{50}$ ) and test this model on the test dataset ( $testAP_{50}$ ).

- Single frame: training the general model with single frame as the input.
- Two frames: training the pseudo siamese model with two adjacent frames ( $I_f, I_{f-1}$ ). In this situation, the DFA degenerates to  $h_{agg} = h_{bn} + h_{bdn}$ .

**Table 3**

Ablation with DETR on the Brainwash dataset.

Input	SFA	DFA	APC	$valAP_{50}$	$testAP_{50}$	Params
Single frame				0.509	0.525	344.9M
Two frames		$\oplus$		0.783	0.713	477.8M
Diffabs		$\oplus$		0.723	0.713	389.7M
Diffabs		$\ominus$		0.774	<b>0.762</b>	477.8M

- Diffabs: using pre-computed sequence pairs ( $I_f, I_{df}$ ) to train the pseudo siamese model with the  $f$ -th frame ground truth.
- DFA: two variants of DFA are considered, where  $\ominus$  represents using our Eq. (5) to aggregate the deep features, and  $\oplus$  represents using the simple addition.

We test MPSN among different backbone networks (VGGNet16, MobileNetv2, Resnet18). In each backbone network and dataset, we fix hyperparameters to fairly compare single frame, two frames, and MPSN methods. The results in Table 2 show MPSN achieves superior performance on two datasets. It means that MPSN does not rely on fixed network architectures, thus it can be flexibly applied in each CNN-based detection framework with high accuracy.

In particular, as for "MobileNetv2" on the Restaurant dataset, the single frame method achieves a reasonable performance of 0.785 AP. Simultaneously, the two frames method achieves similar accuracy of 0.808 AP. After applying MPSN, we achieve the AP 0.838 with the same hyperparameters. This significant improvement means that MPSN can guide CNN to extract motion features effectively, resulting in higher accuracy.

In addition, to verify the flexibility, we also apply our MPSN in the DETR framework, which detects objects using a transformer. The DETR with ResNet18 is compared in Table 3. In our experiments, we only add DFA in the ResNet18 backbone network before the transformer decoder. The Diffabs and two frames methods (0.713 AP) have been significantly improved. It means that the additional information can help the performance. Importantly, compared with the two frames situation at the same scale of model parameters, our Diffabs and DFA method achieve 0.762 AP, about 6.87% improvement. It benefits from the crafty design of DFA and the effective use of motion information. However, the transformer decoder has more parameters, which is not applicable in practice. In contrast, since the MobileNetv2 backbone network has fewer parameters and computational complexity (Sandler et al., 2018), it is suitable for edge deployments.

#### 4.4. Diffabs versus Flow

Optical flow is widely used in video analysis and processing. We compare optical flow and frame difference in this part. We utilize the state-of-the-art (SOTA) optical flow estimation method named RAFT (Teed and Deng, 2020) to extract flow images, which are the inputs to our MPSN. The frame difference is simply implemented by subtraction

**Table 4**

Comparison of Diffabs against Flow on the two datasets.

Dataset	Network	Flow		Diffabs	
		$valAP_{50}$	$testAP_{50}$	$valAP_{50}$	$testAP_{50}$
Restaurant	VGGNet16	0.789	0.812	<b>0.816</b>	<b>0.857</b>
	MobileNetv2	<b>0.759</b>	0.790	0.752	<b>0.838</b>
	Resnet18	0.743	0.793	<b>0.747</b>	<b>0.802</b>
Brainwash	VGGNet16	0.866	0.903	<b>0.884</b>	<b>0.909</b>
	MobileNetv2	0.865	0.880	<b>0.867</b>	<b>0.899</b>
	Resnet18	0.850	0.880	<b>0.852</b>	<b>0.885</b>

and absolute value operators. In this experiment, we fix DFA, APC, and hyperparameters to compare Diffabs and Flow fairly. The results are shown in Table 4. It can be seen that Diffabs achieves better performance than Flow in most situations, regardless of datasets and backbone networks. Note that the SOTA optical flow estimation method has more complex computation and more parameters than the simple frame difference method. In conclusion, as compared to Flow-based methods, the Diffabs-based methods have lower computational requirements while enjoying higher accuracy.

#### 4.5. An application: occupancy counting

An application of MPSN is occupancy counting, which is the core component of occupancy-based control in buildings. As a critical perception algorithm, MPSN provides the number of occupants, which can be applied to control the HVAC and lighting systems. For example, energy can be effectively saved and indoor air environment quality can be improved, through adjusting the opening rate of air dampers dynamically according to the number of indoor people. In this experiment, we will apply MPSN to evaluate the performance of indoor occupancy counting. (In practice, balancing the low computational complexity and high accuracy, we choose the MobileNetv2 backbone (Sandler et al., 2018) as the test model.)

We define two evaluation indicators for occupancy counting as follows:

$$\begin{aligned}
NMAE &= \frac{1}{N} \sum_{f=1}^N \frac{|n_f - \bar{n}_f|}{n_f + \bar{n}_f}, \\
SCORE &= \frac{1}{N} \sum_{f=1}^N (1 - \text{sign}|n_f - \bar{n}_f|),
\end{aligned} \tag{8}$$

where  $n_f$  represents the true number of people (ground truth) in the  $f_{th}$  frame. And  $\bar{n}_f$  represents the predicted number of people (predicted value) in the  $f_{th}$  frame. The ground truth of the video is obtained manually, while the predicted value is output by MPSN.  $\text{sign}$  represents the sign function.

The Normalized Mean Absolute Error ( $NMAE \in [0, 1]$ ) is calculated through the absolute difference between  $n_f$  and  $\bar{n}_f$ . We normalized it because the occupancy counting error increases with the people number rise (Sun et al., 2020). The SCORE is the rate of ground truth is equal to the

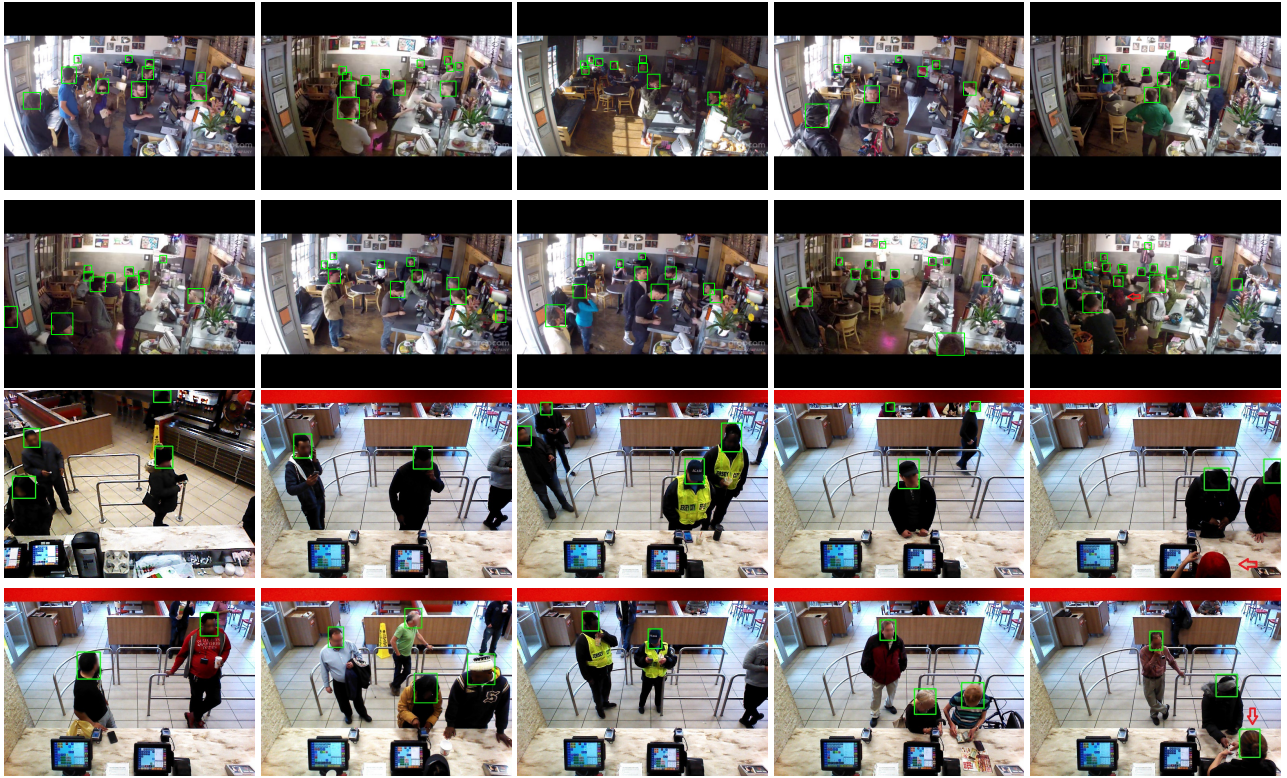


**Figure 3:** Qualitative results of MPSN on the test set of the Brainwash dataset and the Restaurant dataset. In the first four columns, we present successful results where all human heads are detected accurately even though several heads are tiny. In the last column, we provide some failure instances. As marked by red arrows in pictures, three heads are missed because of severe occlusion: such as a back-view red hair woman, and a red cap, while a head is not located accurately. They are hard to be discovered even with human eyes.

**Table 5**

Performance of occupancy counting.

Dataset	NMAE	SCORE	Avg head counting
Restaurant	0.125	0.525	2.549
Brainwash	0.125	0.186	10.345

predicted value (hit rate). We expect the NMAE to be smaller and the SCORE to be bigger.

In Table 5, the Avg head counting is the average occupancy counting in the test head dataset. From it, the NMAE does not change even though the average numbers of people are significantly different on the two datasets. It partially shows that our NMAE is insensitive to the scale of occupants. On the other hand, the small NMAE indicates the MPSN has a good performance of occupancy counting, as shown in Fig. 3. Intuitively, if the true number of people ( $n_f$ ) is 5, with the 0.125 NMAE, the predicted number ( $\bar{n}_f$ ) will be 4 or 6 statistically. This small error can be tolerated for coarse-grained building control. Note that MPSN is only the head detector, thus post-processing and pre-processing methods are able to cascaded to improve the counting performance. These processing methods (such as max counting algorithm (Choi et al., 2021a), clustering analyzer (Zou et al., 2017)

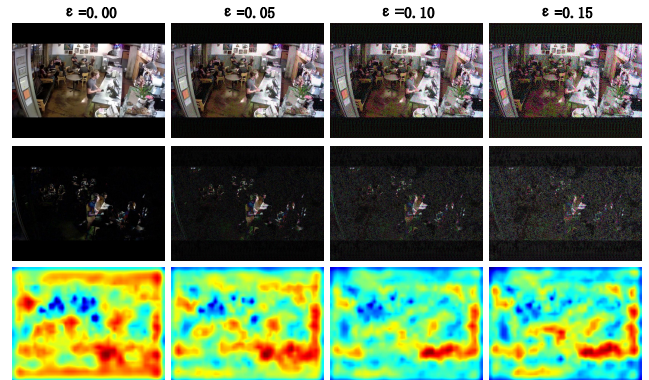


**Figure 4:** Visualization of the effects of increasing adversarial perturbation. The first row represents the adversarial images; the second row represents the motion in adversarial images; the last row represents the CAM heatmaps from the last CNN layer.

and occupancy frequency histogram (Sun et al., 2022)) are beyond the scope of this paper.

#### 4.6. Robustness to adversarial samples

Recent studies in adversarial samples (Akhtar and Mian, 2018) find imperceptible perturbations in input images can completely fool the deep learning models. We conduct an experiment on robustness with adversarial samples. Instead

of defending the adversarial attacks, the purpose of this experiment is to evaluate the robustness of MPSN. We add adversarial perturbations to our dataset, which are computed by the Fast Gradient Sign Method (FGSM) (Goodfellow, Shlens and Szegedy, 2015):

$$\begin{aligned} \mathbf{I}_f^a &= \mathbf{I}_f + \epsilon \text{sign}(\nabla_{\mathbf{I}_f} L(\theta, \mathbf{I}_f, y_f)), \\ \mathbf{I}_{f-1}^a &= \mathbf{I}_{f-1} + \epsilon \text{sign}(\nabla_{\mathbf{I}_{f-1}} L(\theta, \mathbf{I}_{f-1}, y_{f-1})), \end{aligned} \quad (9)$$

where  $\epsilon \in [0, 1]$ . In Fig. 5, with the  $\epsilon$  increasing, the attack effect also increases; thus the  $AP_{50}$  decreases. It is worth noting that the  $AP_{50}$  of MPSN is always higher than FCHD among different  $\epsilon$ . It means that no matter how great this attack is, MPSN can achieve a better performance compared with FCHD. At  $\epsilon = 0$  level, the attack effects disappear. At  $\epsilon = 0.4$  level, MPSN converges to higher accuracy. Correspondingly, the detailed effects against adversarial perturbations are visualized in Fig. 4. In fact, to some extent, the blue areas in heatmaps can represent the head positions. It can be seen that with the increasing perturbations, the heatmaps become inaccurate, which confirms the decrease of AP in Fig. 5. However, it looks like that the second row (frame difference) is less affected by the perturbations because the motion area is significant. Perhaps it reduces the perturbations and results in the higher accuracy in Fig. 5.

We utilize the Non-I.I.D. Index (NI) (He, Shen and Cui, 2021) to evaluate the robustness in Fig. 5:

$$\begin{aligned} NI_{MPSN} &= \left\| \frac{\overline{g_\theta(\mathbf{I}^a, \mathbf{I}_d^a)} - \overline{g_\theta(\mathbf{I}, \mathbf{I}_d)}}{\text{std}(g_\theta(\mathbf{I}^a, \mathbf{I}_d^a) \cup g_\theta(\mathbf{I}, \mathbf{I}_d))} \right\|_2, \\ NI_{FCHD} &= \left\| \frac{\overline{g_\varphi(\mathbf{I}^a)} - \overline{g_\varphi(\mathbf{I})}}{\text{std}(g_\varphi(\mathbf{I}^a) \cup g_\varphi(\mathbf{I}))} \right\|_2, \end{aligned} \quad (10)$$

and

$$\begin{aligned} \overline{g_\theta(\mathbf{I}^a, \mathbf{I}_d^a)} &= \frac{1}{N} \sum_{f=1}^N g_\theta(\mathbf{I}_f^a, \mathbf{I}_{df}^a), \\ \overline{g_\varphi(\mathbf{I}^a)} &= \frac{1}{N+1} \sum_{f=0}^N g_\varphi(\mathbf{I}_f^a), \end{aligned} \quad (11)$$

where  $g_\theta$  represents the feature extractor of MPSN and  $g_\varphi$  represents the feature extractor of FCHD. The superscript  $\mathbf{a}$  represents the input image after attack,  $\overline{(\cdot)}$  represents the first order moment,  $\text{std}$  is the standard deviation function and  $\|\cdot\|_2$  represents the 2-norm. Eq. (10) measures the feature difference between original images and adversarial samples.

Since MPSN and FCHD have different network architectures, we slightly modified the NI as follows:

$$\begin{aligned} NI_{MPSN} &= \left\| \frac{\overline{CAM(\mathbf{h}_{det}^a)} - \overline{CAM(\mathbf{h}_{det})}}{\text{std}(CAM(\mathbf{h}_{det}^a) \cup CAM(\mathbf{h}_{det}))} \right\|_2, \\ NI_{FCHD} &= \left\| \frac{\overline{CAM(\mathbf{d}_{det}^a)} - \overline{CAM(\mathbf{d}_{det})}}{\text{std}(CAM(\mathbf{d}_{det}^a) \cup CAM(\mathbf{d}_{det}))} \right\|_2, \end{aligned} \quad (12)$$

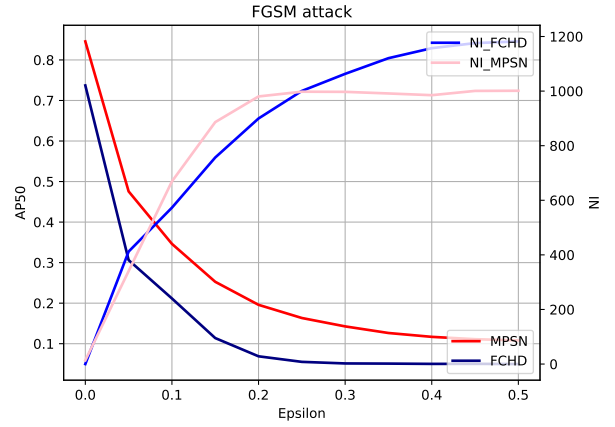


**Figure 5:** Comparison of the robustness between MPSN and FCHD under adversarial noise.

where  $\mathbf{h}_{det}$  and  $\mathbf{d}_{det}$  represents the features from the last CNN layer of MPSN and FCHD, respectively. The main advantage of  $CAM$  is interpretability. Thus we specify the  $CAM$  heatmap from the last CNN layer as  $g(\cdot)$  function..

The comparing results are shown in Fig. 5. The strong correlation between NI and testing error has been proved in (He et al., 2021). It seems that FCHD is more robust than MPSN if  $\epsilon \in [0.07, 0.25]$ . It can be explained that the AP decrease of MPSN is serious. However, in applications, we focus on the small  $\epsilon$  because the great perturbations violate small input changes even destroy the original image (Feinman, Curtin, Shintre and Gardner, 2017). According to Fig. 5, if  $\epsilon \leq 0.07$ , MPSN is more robust and accurate than FCHD. In this situation, we are more likely to apply MPSN in real systems. On the other hand, if  $\epsilon \geq 0.07$ , we may choose FCHD. So the threshold is very important to select the more robust model and further guide the applications. While the threshold is experimental, we further discuss the mathematical solution of the small  $\epsilon$  in the Appendix.

## 5. CONCLUSIONS

In this work, we present MPSN to suppress false positives and recover missed detection in video head detection. We design SFA and DFA by introducing motion information, guiding the pseudo siamese model to extract robust head motion features. Experimental results show that MPSN achieves higher performance on the two challenging datasets. Experiments based on different backbone networks (VGGNet16, MobileNetv2, Resnet18) verify the flexibility of MPSN. Compared with optical flow-based methods, our Diffabs-based methods have lower computational requirements and higher accuracy in experiments. Adversarial samples are implemented to evaluate the robustness of MPSN. We also provide the mathematical solution of small perturbations to select more robust models. We hope our study can promote the application of the deep learning model in real-world video applications.



## 6. Funding

This work is supported by Key R&D Project of China under Grant No. 2017YFC0704100, 2016YFB0901900, National Natural Science Foundation of China under Grant No. 62192751 and 61425024, the 111 International Collaboration Program of China under Grant No. BP2018006, 2019 Major Science and Technology Program for the Strategic Emerging Industries of Fuzhou under Grant No. 2019-Z-1, and in part by the BNRist Program under Grant No. BNR2019TD01009, the National Innovation Center of High Speed Train R&D project (CX/KJ-2020-0006).

## References

- Acquaah, Y., Steele, J.B., Gokaraju, B., Tesiero, R., Monty, G.H., 2020. Occupancy detection for smart hvac efficiency in building energy: A deep learning neural network framework using thermal imagery, in: 2020 IEEE Applied Imagery Pattern Recognition Workshop (AIPR), IEEE. pp. 1–6.
- Aftab, M., Chen, C., Chau, C.K., Rahwan, T., 2017. Automatic hvac control with real-time occupancy recognition and simulation-guided model predictive control in low-cost embedded system. *Energy and Buildings* 154, 141–156. URL: <https://www.sciencedirect.com/science/article/pii/S0378778817305091>, doi:<https://doi.org/10.1016/j.enbuild.2017.07.077>.
- Akhtar, N., Mian, A., 2018. Threat of adversarial attacks on deep learning in computer vision: A survey. *Ieee Access* 6, 14410–14430.
- Babu Sam, D., Surya, S., Venkatesh Babu, R., 2017. Switching convolutional neural network for crowd counting, in: Proceedings of the IEEE conference on computer vision and pattern recognition, pp. 5744–5752.
- Benezeth, Y., Laurent, H., Emile, B., Rosenberger, C., 2011. Towards a sensor for detecting human presence and characterizing activity. *Energy and Buildings* 43, 305–314. URL: <https://www.sciencedirect.com/science/article/pii/S0378778810003348>, doi:<https://doi.org/10.1016/j.enbuild.2010.09.014>.
- Carion, N., Massa, F., Synnaeve, G., Usunier, N., Kirillov, A., Zagoruyko, S., 2020. End-to-End Object Detection with Transformers, in: Computer Vision - ECCV 2020. 16th European Conference. Proceedings. Lecture Notes in Computer Science (LNCS 12346), pp. 213–29.
- Chandran, A.K., Wong, W.C., Ieee, 2016. Pedestrian Crowd Level Estimation by Head Detection using Bio-inspired Retina Model. Proceedings of the 2016 Ieee Region 10 Conference.
- Chen, K., Pang, J., Wang, J., Xiong, Y., Li, X., Sun, S., Feng, W., Liu, Z., Shi, J., Ouyang, W., et al., 2019. Hybrid task cascade for instance segmentation, in: Proceedings of the IEEE/CVF Conference on Computer Vision and Pattern Recognition, pp. 4974–4983.
- Chi, C., Zhang, S., Xing, J., Lei, Z., Li, S.Z., Zou, X., 2020. Relational learning for joint head and human detection, in: Proceedings of the AAAI Conference on Artificial Intelligence, pp. 10647–10654.
- Choi, H., Um, C.Y., Kang, K., Kim, H., Kim, T., 2021a. Application of vision-based occupancy counting method using deep learning and performance analysis. *Energy and Buildings* 252, 111389.
- Choi, H., Um, C.Y., Kang, K., Kim, H., Kim, T., 2021b. Review of vision-based occupant information sensing systems for occupant-centric control. *Building and Environment* 203, 108064.
- Chouai, M., Dolezel, P., Stursa, D., Nemeč, Z., 2021. New end-to-end strategy based on deeplabv3+ semantic segmentation for human head detection. *Sensors* 21, 5848.
- Dai, J., Li, Y., He, K., Sun, J., 2016. R-fcn: Object detection via region-based fully convolutional networks. *Advances in neural information processing systems* 29.
- Dai, X., Chen, Y., Yang, J., Zhang, P., Yuan, L., Zhang, L., 2021. Dynamic detr: End-to-end object detection with dynamic attention, in: Proceedings of the IEEE/CVF International Conference on Computer Vision, pp. 2988–2997.
- Dino, I., Kalfaoglu, E., Sari, A., Akin, S., Iseri, O., Alatan, A., Kalkan, S., Erdogan, B., 2019. Video content analysis-based detection of occupant presence for building energy modelling. *Advances in ICT in Design, Construction and Management in Architecture, Engineering, Construction and Operations (AECO)*, Northumbria University (9 2019), 974–985.
- Duan, K., Bai, S., Xie, L., Qi, H., Huang, Q., Tian, Q., 2019. CenterNet: Keypoint triplets for object detection, in: Proceedings of the IEEE/CVF international conference on computer vision, pp. 6569–6578.
- El Ahmar, W.A., Erlik Nowruz, F., Laganieri, R., 2020. Fast human head and shoulder detection using convolutional networks and rgbd data, in: 2020 IEEE/CVF Conference on Computer Vision and Pattern Recognition Workshops (CVPRW), pp. 479–487. doi:10.1109/CVPRW50498.2020.00061.
- Feinman, R., Curtin, R.R., Shintre, S., Gardner, A.B., 2017. Detecting adversarial samples from artifacts. *arXiv:1703.00410*.
- Ge, Z., Liu, S., Wang, F., Li, Z., Sun, J., 2021. YOLOX: exceeding YOLO series in 2021. *CoRR abs/2107.08430*. URL: <https://arxiv.org/abs/2107.08430>, arXiv:2107.08430.
- Goodfellow, I.J., Shlens, J., Szegedy, C., 2015. Explaining and harnessing adversarial examples. *arXiv:1412.6572*.
- Granger, E., Kiran, M., Blais-Morin, L.A., et al., 2017. A comparison of cnn-based face and head detectors for real-time video surveillance applications, in: 2017 Seventh International Conference on Image Processing Theory, Tools and Applications (IPTA), IEEE. pp. 1–7.
- Guan, Y., Huang, Y., 2015. Multi-pose human head detection and tracking boosted by efficient human head validation using ellipse detection. *Engineering Applications of Artificial Intelligence* 37, 181–193. URL: <https://www.sciencedirect.com/science/article/pii/S0952197614002036>, doi:<https://doi.org/10.1016/j.engappai.2014.08.004>.
- Han, W., Khorrami, P., Paine, T.L., Ramachandran, P., Babaeizadeh, M., Shi, H., Li, J., Yan, S., Huang, T.S., 2016. Seq-nms for video object detection. *CoRR abs/1602.08465*.
- He, K., Zhang, X., Ren, S., Sun, J., 2015. Deep residual learning for image recognition. *CoRR abs/1512.03385*. URL: <http://arxiv.org/abs/1512.03385>, arXiv:1512.03385.
- He, Y., Shen, Z., Cui, P., 2021. Towards non-i.i.d. image classification: A dataset and baselines. *Pattern Recognition* 110, 107383. URL: <https://www.sciencedirect.com/science/article/pii/S0031320320301862>, doi:<https://doi.org/10.1016/j.patcog.2020.107383>.
- Held, D., Thrun, S., Savarese, S., 2016. Learning to track at 100 fps with deep regression networks, in: European conference on computer vision, Springer. pp. 749–765.
- Huang, Q., Hao, K., 2020. Development of cnn-based visual recognition air conditioner for smart buildings. *J. Inf. Technol. Constr.* 25, 361–373.
- Hughes, L.H., Schmitt, M., Mou, L., Wang, Y., Zhu, X.X., 2018. Identifying corresponding patches in sar and optical images with a pseudo-siamese cnn. *IEEE Geoscience and Remote Sensing Letters* 15, 784–788.
- Ilg, E., Mayer, N., Saikia, T., Keuper, M., Dosovitskiy, A., Brox, T., 2017. FlowNet 2.0: Evolution of optical flow estimation with deep networks, in: Proceedings of the IEEE conference on computer vision and pattern recognition, pp. 2462–2470.
- Jia, Q.S., Zhang, C., Liu, Z., 2019. A distributed occupancy distribution estimation method for smart buildings, in: 2019 IEEE 15th International Conference on Control and Automation (ICCA), IEEE. pp. 211–216.
- Ke, R., Zhuang, Y., Pu, Z., Wang, Y., 2020. A smart, efficient, and reliable parking surveillance system with edge artificial intelligence on iot devices. *IEEE Transactions on Intelligent Transportation Systems* 22, 4962–4974.
- Khan, S., Naseer, M., Hayat, M., Zamir, S.W., Khan, F.S., Shah, M., 2021. Transformers in vision: A survey. *ACM Computing Surveys (CSUR)*.
- Khan, S.D., Ali, Y., Zafar, B., Noorwali, A., 2020. Robust head detection in complex videos using two-stage deep convolution framework. *IEEE Access* 8, 98679–98692.
- Khan, S.D., Altamimi, A.B., Ullah, M., Ullah, H., Cheikh, F.A., 2020. TCM: Temporal Consistency Model for Head Detection in Complex Videos.

- JOURNAL OF SENSORS 2020. doi:{10.1155/2020/8861296}.
- Khan, S.D., Ullah, H., Uzair, M., Ullah, M., Ullah, R., Cheikh, F.A., 2019. Density independent and scale aware model for crowd counting and localization, pp. 4474–4478.
- Li, J., Wang, Y., Wang, C., Tai, Y., Qian, J., Yang, J., Wang, C., Li, J., Huang, F., 2019. Dsfd: dual shot face detector, in: Proceedings of the IEEE/CVF Conference on Computer Vision and Pattern Recognition, pp. 5060–5069.
- Lin, T.Y., Goyal, P., Girshick, R., He, K., Dollár, P., 2017. Focal loss for dense object detection, in: Proceedings of the IEEE international conference on computer vision, pp. 2980–2988.
- Liu, J., Zhang, Y., Xie, J., Wei, Y., Wang, Z., Niu, M., 2021a. Head detection based on dr feature extraction network and mixed dilated convolution module. *Electronics* 10, 1565.
- Liu, Y., Zhang, X.Y., Bian, J.W., Zhang, L., Cheng, M.M., 2021b. Samnet: Stereoscopically attentive multi-scale network for lightweight salient object detection. *IEEE Transactions on Image Processing* 30, 3804–3814.
- Lucas, B.D., Kanade, T., et al., 1981. An iterative image registration technique with an application to stereo vision, Vancouver, British Columbia.
- Meng, Y.b., Li, T.y., Liu, G.h., Xu, S.j., Ji, T., 2020. Real-time dynamic estimation of occupancy load and an air-conditioning predictive control method based on image information fusion. *Building and Environment* 173, 106741.
- Mutis, I., Ambekar, A., Joshi, V., 2020. Real-time space occupancy sensing and human motion analysis using deep learning for indoor air quality control. *Automation in Construction* 116, 103237. URL: <https://www.sciencedirect.com/science/article/pii/S0926580519307630>, doi:<https://doi.org/10.1016/j.autcon.2020.103237>.
- Pang, Z., Chen, Y., Zhang, J., O'Neill, Z., Cheng, H., Dong, B., 2020. Nationwide hvac energy-saving potential quantification for office buildings with occupant-centric controls in various climates. *Applied Energy* 279, 115727. URL: <https://www.sciencedirect.com/science/article/pii/S0306261920312186>, doi:<https://doi.org/10.1016/j.apenergy.2020.115727>.
- Ren, S., He, K., Girshick, R., Sun, J., 2015. Faster r-cnn: Towards real-time object detection with region proposal networks. *Advances in neural information processing systems* 28.
- Salimi, S., Hammad, A., 2019. Critical review and research roadmap of office building energy management based on occupancy monitoring. *Energy and Buildings* 182, 214–241.
- Sandler, M., Howard, A.G., Zhu, M., Zhmoginov, A., Chen, L., 2018. Inverted residuals and linear bottlenecks: Mobile networks for classification, detection and segmentation. *CoRR abs/1801.04381*.
- Shen, W., Qin, P., Zeng, J., 2019. An indoor crowd detection network framework based on feature aggregation module and hybrid attention selection module, in: Proceedings of the IEEE/CVF International Conference on Computer Vision Workshops, pp. 0–0.
- Simonyan, K., Zisserman, A., 2015. Very deep convolutional networks for large-scale image recognition, in: International Conference on Learning Representations.
- Stewart, R., Andriluka, M., Ng, A.Y., 2016. End-to-end people detection in crowded scenes, in: Proceedings of the IEEE conference on computer vision and pattern recognition, pp. 2325–2333.
- Sun, K., Zhao, Q., Zhang, Z., Hu, X., 2022. Indoor occupancy measurement by the fusion of motion detection and static estimation. *Energy and Buildings* 254, 111593. URL: <https://www.sciencedirect.com/science/article/pii/S037877882100877X>, doi:<https://doi.org/10.1016/j.enbuild.2021.111593>.
- Sun, K., Zhao, Q., Zou, J., 2020. A review of building occupancy measurement systems. *Energy and Buildings* 216, 109965. URL: <https://www.sciencedirect.com/science/article/pii/S0378778819332918>, doi:<https://doi.org/10.1016/j.enbuild.2020.109965>.
- Teed, Z., Deng, J., 2020. Raft: Recurrent all-pairs field transforms for optical flow, in: European conference on computer vision, Springer. pp. 402–419.
- Tien, P.W., Wei, S., Calautit, J.K., Darkwa, J., Wood, C., 2022. Real-time monitoring of occupancy activities and window opening within buildings using an integrated deep learning-based approach for reducing energy demand. *Applied Energy* 308, 118336. URL: <https://www.sciencedirect.com/science/article/pii/S0306261921015865>, doi:<https://doi.org/10.1016/j.apenergy.2021.118336>.
- Trivedi, D., Badarla, V., 2020. Occupancy detection systems for indoor environments: A survey of approaches and methods. *Indoor and Built Environment* 29, 1053–1069.
- Viola, P., Jones, M., 2001. Rapid object detection using a boosted cascade of simple features, in: Proceedings of the 2001 IEEE Computer Society Conference on Computer Vision and Pattern Recognition. CVPR 2001, pp. I–511–18 vol.1.
- Vu, T.H., Osokin, A., Laptev, I., 2015. Context-aware CNNs for person head detection, in: 2015 IEEE INTERNATIONAL CONFERENCE ON COMPUTER VISION (ICCV), pp. 2893–2901. IEEE International Conference on Computer Vision, Santiago, CHILE, DEC 11–18, 2015.
- Wang, J., Huang, J., Feng, Z., Cao, S.J., Haghghat, F., 2021. Occupant-density-detection based energy efficient ventilation system: Prevention of infection transmission. *Energy and Buildings* 240, 110883. URL: <https://www.sciencedirect.com/science/article/pii/S0378778821001675>, doi:<https://doi.org/10.1016/j.enbuild.2021.110883>.
- Wang, S., Zhou, Y., Yan, J., Deng, Z., 2018. Fully motion-aware network for video object detection, in: Ferrari, V., Hebert, M., Sminchisescu, C., Weiss, Y. (Eds.), *Computer Vision – ECCV 2018*, Springer International Publishing, Cham. pp. 557–573.
- Woo, S., Park, J., Lee, J.Y., Kweon, I.S., 2018. Cbam: Convolutional block attention module, in: Proceedings of the European conference on computer vision (ECCV), pp. 3–19.
- Wu, C., Zhang, Y., Zhang, Y., Zhang, W., Wang, H., Zhang, Y., Sun, X., 2020. Motion guided siamese trackers for visual tracking. *IEEE Access* 8, 7473–7489. doi:10.1109/ACCESS.2020.2964269.
- Xiang, J., Zhu, G., 2017. Joint face detection and facial expression recognition with mtcnn, in: 2017 4th international conference on information science and control engineering (ICISCE), IEEE. pp. 424–427.
- Zhou, B., Khosla, A., Lapedriza, A., Oliva, A., Torralba, A., 2016. Learning deep features for discriminative localization, in: Proceedings of the IEEE conference on computer vision and pattern recognition, pp. 2921–2929.
- Zhu, X., Dai, J., Yuan, L., Wei, Y., 2018. Towards high performance video object detection, in: Proceedings of the IEEE Conference on Computer Vision and Pattern Recognition, pp. 7210–7218.
- Zou, J., Zhao, Q., Yang, W., Wang, F., 2017. Occupancy detection in the office by analyzing surveillance videos and its application to building energy conservation. *Energy and Buildings* 152, 385–398. doi:10.1016/j.enbuild.2017.07.064.

**Table 6**

Architectures of backbone network.

Backbone	VGGNet16	MobileNetv2	Resnet18
$N_{FN}/N_{FDN}$	conv1	conv1	conv1
	conv2	bottleneck1-3	conv2_x
$N_{BN}/N_{BDN}$	conv3		conv3_x
	conv4	bottleneck4-13	conv4_x
	conv5		

## A. Appendix

### A.1. Network architectures and hyperparameters

We use the modified FCHD as our detection network in Section 3. The VGGNet16, MobileNetv2, and Resnet18 backbone networks are applied for comparison. The detailed network architectures of them we utilized as shown in Table 6. The architecture of  $N_{FDN}$  is the same as  $N_{FN}$ 's, but the weights will be updated separately. If the resolution of the original image is  $H \times W$ , it will decrease to  $H/4 \times W/4$  after  $N_{FN}$  and  $N_{FDN}$ . Similarly, the resolution will decrease to  $H/16 \times W/16$  after  $N_{BN}$  and  $N_{BDN}$ . The entire model is trained by the SGD optimizer for 50 epochs. The learning rate is  $10^{-2}$  and is decayed as  $10^{-3}$ ,  $10^{-4}$  and  $10^{-5}$  after 15, 35 and 42 epochs separately. MPSN is also tested on DETR. We select the Resnet18 as the backbone network, then add a pseudo siamese network and DFA to compare the detection performance. The model is trained for 300 epochs. The learning rate of the backbone network is set to  $10^{-5}$  and is decayed as  $10^{-6}$  and  $10^{-7}$  after 100 and 200 epochs separately. The batchsize is set to 1.

### A.2. The mathematical solution of small $\epsilon$

According to the Eq. (1) and Eq. (9), we have

$$\begin{aligned} I_{df}^a &= |I_f^a - I_{f-1}^a| \\ &= |I_f - I_{f-1} + \epsilon[\text{sign}(\nabla_{I_f} L(\theta, I_f, y_f)) \\ &\quad - \text{sign}(\nabla_{I_{f-1}} L(\theta, I_{f-1}, y_{f-1}))]|, \end{aligned}$$

thus,

$$\begin{aligned} I_{df}^a - I_{df} &\leq |I_f - I_{f-1}| + \epsilon|\text{sign}(\nabla_{I_f} L(\theta, I_f, y_f)) \\ &\quad - \text{sign}(\nabla_{I_{f-1}} L(\theta, I_{f-1}, y_{f-1}))| - |I_f - I_{f-1}| \\ &= \epsilon|\text{sign}(\nabla_{I_f} L(\theta, I_f, y_f)) - \text{sign}(\nabla_{I_{f-1}} L(\theta, I_{f-1}, y_{f-1}))|, \end{aligned}$$

$$\begin{aligned} I_{df}^a - I_{df} &\geq |I_f - I_{f-1}| - \epsilon|\text{sign}(\nabla_{I_f} L(\theta, I_f, y_f)) \\ &\quad - \text{sign}(\nabla_{I_{f-1}} L(\theta, I_{f-1}, y_{f-1}))| - |I_f - I_{f-1}| \\ &= -\epsilon|\text{sign}(\nabla_{I_f} L(\theta, I_f, y_f)) - \text{sign}(\nabla_{I_{f-1}} L(\theta, I_{f-1}, y_{f-1}))|. \end{aligned}$$

Let  $t = |\text{sign}(\nabla_{I_f} L(\theta, I_f, y_f)) - \text{sign}(\nabla_{I_{f-1}} L(\theta, I_{f-1}, y_{f-1}))|$ , thus,

$$-\epsilon t \geq I_{df}^a - I_{df} \leq \epsilon t. \quad (13)$$

Because  $\epsilon$  is small in applications, we conduct Taylor expansion at  $I_f$ :

$$\begin{aligned} g_\varphi(I_f^a) - g_\varphi(I_f) &= \frac{\partial g_\varphi(I_f)}{\partial I_f} (I_f^a - I_f) + \frac{\partial^2 g_\varphi(I_f)}{2\partial I_f^2} (I_f^a \\ &\quad - I_f)^2 + O(\epsilon^3) \approx \epsilon \frac{\partial g_\varphi(I_f)}{\partial I_f} \text{sign}(\nabla_{I_f} L(\varphi, I_f, y_{f-1})) + \\ &\quad \frac{\epsilon^2}{2} \text{sign}^\top(\nabla_{I_f} L(\varphi, I_f, y_{f-1})) \frac{\partial^2 g_\varphi(I_f)}{2\partial I_f^2} \text{sign}(\nabla_{I_f} L(\varphi, I_f, y_{f-1})). \end{aligned}$$

Similarly, we conduct Multiple Taylor expansion at  $I_f, I_{df}$ :

$$\begin{aligned} g_\theta(I_f^a, I_{df}^a) - g_\theta(I_f, I_{df}) &= \frac{\partial g_\theta(I_f, I_{df})}{\partial I_f} (I_f^a - I_f) + \\ &\quad \frac{\partial g_\theta(I_f, I_{df})}{\partial I_{df}} (I_{df}^a - I_{df}) + \frac{1}{2} [(I_f^a - I_f)^\top (I_{df}^a - I_{df})^\top] \\ &\quad \begin{bmatrix} \frac{\partial^2 g_\theta(I_f, I_{df})}{\partial I_f^2} & \frac{\partial^2 g_\theta(I_f, I_{df})}{\partial I_f \partial I_{df}} \\ \frac{\partial^2 g_\theta(I_f, I_{df})}{\partial I_{df} \partial I_f} & \frac{\partial^2 g_\theta(I_f, I_{df})}{\partial I_{df}^2} \end{bmatrix} \begin{bmatrix} (I_f^a - I_f) \\ (I_{df}^a - I_{df}) \end{bmatrix} + O(\epsilon^3) \\ &\leq \epsilon \frac{\partial g_\theta(I_f, I_{df})}{\partial I_f} \text{sign}(\nabla_{I_f} L(\theta, I_f, y_f)) + \epsilon \left| \frac{\partial g_\theta(I_f, I_{df})}{\partial I_{df}} \right| \\ &\quad t + \frac{\epsilon^2}{2} \text{sign}^\top(\nabla_{I_f} L(\theta, I_f, y_f)) \frac{\partial^2 g_\theta(I_f, I_{df})}{\partial I_f^2} \text{sign}(\nabla_{I_f} L(\theta, \\ &\quad I_f, y_f)) + \epsilon^2 |\text{sign}^\top(\nabla_{I_f} L(\theta, I_f, y_f)) \frac{\partial^2 g_\theta(I_f, I_{df})}{\partial I_f \partial I_{df}}| t \\ &\quad + \frac{\epsilon^2}{2} t^\top \frac{\partial^2 g_\theta(I_f, I_{df})}{\partial I_{df}^2} t. \end{aligned}$$

When  $NI\_MPSN \leq NI\_FCHD$ :

$$\begin{aligned} &\left\| \frac{1}{NC} \sum_{f=1}^N [g_\theta(I_f^a, I_{df}^a) - g_\theta(I_f, I_{df})] \right\|_2 \\ &\leq \left\| \frac{1}{(N+1)D} \sum_{f=0}^N [g_\varphi(I_f^a) - g_\varphi(I_f)] \right\|_2. \end{aligned} \quad (14)$$

Both sides are quadratic functions of  $\epsilon$ , thus,

$$|j\epsilon + \epsilon^2 k| \leq |l\epsilon + \epsilon^2 m| \Rightarrow |j + \epsilon k| \leq |l + \epsilon m|. \quad (15)$$

The small  $\epsilon$  can be obtained mathematically.